

MULTI-DIMENSIONAL RADIATION/HYDRODYNAMIC SIMULATIONS OF PROTONEUTRON STAR CONVECTION

L. DESSART¹, A. BURROWS¹, E. LIVNE², C.D. OTT³

Draft version August 15, 2018

ABSTRACT

Based on multi-dimensional, multi-group, flux-limited-diffusion hydrodynamic simulations of core-collapse supernovae with the VULCAN/2D code, we study the physical conditions within and in the vicinity of the nascent protoneutron star (PNS). Our numerical study follows the evolution of the collapsing envelope of the 11- M_{\odot} model of Woosley & Weaver, from ~ 200 ms before bounce to ~ 300 ms after bounce, on a spatial grid that switches from Cartesian at the PNS center to spherical above a 10 km radius.

As has been shown previously, we do not see any large-scale overturn of the inner PNS material. Convection, directly connected to the PNS, is found to occur in two distinct regions: between 10 and 20 km, coincident with the region of negative lepton gradient, and exterior to the PNS above 50 km. Separating these two regions, an interface, with no sizable outward or inward motion, is the site of gravity waves, emerging at ~ 200 -300 milliseconds (ms) after core bounce, excited by the convection in the outer convective zone.

In the PNS, convection is always confined within the neutrinospheric radii for all neutrino energies above just a few MeV. We find that such convective motions do not appreciably enhance the ν_e neutrino luminosity, and that they enhance the $\bar{\nu}_e$ and “ ν_{μ} ” luminosities modestly, by $\sim 15\%$ and $\sim 30\%$, respectively, during the first post-bounce 100–200 ms. Moreover, we see no evidence of doubly-diffusive instabilities in the PNS, expected to operate on diffusion timescales of at least a second, much longer than the millisecond timescale associated with PNS convection.

PNS convection is thus found to be a secondary feature of the core-collapse phenomenon, rather than a decisive ingredient for a successful explosion.

Subject headings: convection – hydrodynamics – neutrinos – stars: neutron – stars: supernovae: general – waves

1. INTRODUCTION

A few million years after the onset of core-hydrogen burning on the main sequence, a massive star creates a degenerate core, which, upon reaching the Chandrasekhar mass, undergoes gravitational collapse. The core infall is eventually halted when its innermost regions reach nuclear densities, generating a shock wave that propagates outwards, initially reversing inflow into outflow. However, detailed numerical radiation-hydrodynamics simulations struggle to produce explosions. Instead of a prompt explosion occurring on a dynamical timescale, simulations produce a stalled shock at ~ 100 -200 km, just a few tens of milliseconds after core bounce: 1D simulations universally yield a stalled shock that ultimately fails to lift off; 2D simulations provide a more divided picture, with success or failure seemingly dependent on the numerical approach or physical assumptions made. Indeed, energy deposition by neutrinos behind the shock, in the so-called gain region, is expected to play a central role in re-energizing the stalled shock: explosion will occur if the shock can be maintained at large-enough radii and for a sufficiently long time to eventually expand into the tenuous infalling en-

velope (Burrows & Goshy 1993). At present, the failure to produce explosions may be due to physical processes not accounted for (e.g., magnetic fields), to an inaccurate treatment of neutrino transport (see the discussion in Buras et al. 2005), or to missing neutrino microphysics.

Because neutrino transport is a key component of the supernovae mechanism in massive stars, slight modifications in the neutrino cooling/heating efficiency could be enough to produce an explosion. Alternatively, an enhancement in the neutrino flux during the first second following core bounce could also lead to a successful explosion. Convection in the nascent protoneutron star (PNS) has been invoked as a potential mechanism for such an increase in the neutrino luminosity. Neutrino escape at and above the neutrinosphere establishes a negative lepton-gradient, a situation unstable to convection under the Ledoux (1947) criterion. Epstein (1979) argued, based on a simulation by Mayle & Wilson (1988), that this leads to large-scale overturn and advection of core regions with high neutrino-energy density at and beyond the neutrinosphere, thereby enhancing the neutrino flux. Such large scale overturn was obtained in simulations by Bruenn, Buchler & Livio (1979) and Livio, Buchler & Colgate (1979), but, as shown by Smarr et al. (1981), their results were compromised by an inadequate equation of state (EOS). Lattimer & Mazurek (1981) challenged the idea of large-scale overturn, noting the presence of a positive, stabilizing entropy gradient - a residue of the shock birth. Thus, while large-scale overturn of the core is unlikely and has thus far never been

¹ Department of Astronomy and Steward Observatory, The University of Arizona, Tucson, AZ 85721; luc@as.arizona.edu, burrows@as.arizona.edu

² Racah Institute of Physics, The Hebrew University, Jerusalem, Israel; eli@frodo.fiz.huji.ac.il

³ Max-Planck-Institut für Gravitationsphysik, Albert-Einstein-Institut, Golm/Potsdam, Germany; cott@aei.mpg.de

seen in realistic simulations of core-collapse supernovae, the possibility of convectively-enhanced neutrino luminosities was still open. Burrows (1987), based on a simple mixing-length treatment, argued that large-scale core-overturn was unlikely, but found neutrino-luminosity enhancements, stemming from convective motions within the PNS, of up to 50%. Subsequently, based on multi-dimensional (2D) radiation hydrodynamics simulations, Burrows, Hayes, & Fryxell (1995) did not find large-scale core overturn, nor any luminosity enhancement, but clearly identified the presence of convection within the PNS, as well as “tsunamis” propagating at its surface. Keil, Janka, & Müller (1996), using a similar approach, reported the presence of both convection and enhancement of neutrino luminosities compared to an equivalent 1D configuration. However, these studies used gray neutrino transport, a spherically-symmetric (1D) description of the inner core (to limit the Courant timestep), and a restriction of the angular coverage to 90° . Keil et al. also introduced a diffusive and moving outer boundary at the surface of the PNS (receding from 60 km down to 20 km, 1 s after core bounce), thereby neglecting any feedback from the fierce convection occurring above, between the PNS surface and the shock radius. Mezzacappa et al. (1998) have performed 2D hydrodynamic simulations of protoneutron star convection, with the option of including neutrino-transport effects as computed from equivalent 1D MGFLD simulations. They found that PNS convection obtains underneath the neutrinosphere in pure hydrodynamical simulations, but that neutrino transport considerably reduces the convection growth rate. We demonstrate in the present work that PNS convection does in fact obtain, even with a (multidimensional) treatment of neutrino transport and that, as these authors anticipated, the likely cause is their adopted 1D radiation transport, which maximizes the lateral equilibration of entropy and lepton number. Recently, Swesty & Myra (2005ab) described simulations of the convective epoch in core-collapse supernovae, using MGFLD neutrino transport, but their 2D study covers only the initial 33 milliseconds (ms) of PNS evolution.

Alternatively, Mayle & Wilson (1988) and Wilson & Mayle (1993) have argued that regions stable to convection according to the Ledoux criterion could be the sites of doubly-diffusive instabilities, taking the form of so-called neutron (low- Y_e material) fingers. This idea rests essentially on the assumption that the neutrino-mediated diffusion of heat occurs on shorter timescales than the neutrino-mediated diffusion of leptons. By contrast, Bruenn & Dineva (1996) and Bruenn, Raley, & Mezzacappa (2005) demonstrated that the neutrino-mediated thermal-diffusion timescale is longer than that of neutrino-mediated lepton-diffusion, and, thus, that neutron fingers do not obtain. Because ν_μ 's and ν_τ 's have a weak thermal coupling to the material, Bruenn, Raley, & Mezzacappa (2005) concluded that lepton-diffusion would occur faster by means of low-energy $\bar{\nu}_e$'s and ν_e 's. Applying their transport simulations to snapshots of realistic core-collapse simulations, they identified the potential for two new types of instabilities within the PNS, referred to as “lepto-entropy fingers” and “lepto-entropy semiconvection”.

In this paper, we present a set of simulations that allow a consistent assessment of dynamical/diffusive/convective mechanisms taking place within the PNS, improving on a number of assumptions made by previous radiation-hydrodynamic investigations. Our approach, based on VULCAN/2D (Livne et al. 2004), has several desirable features for the study of PNS convection.

First, the 2D evolution of the inner 3000-4000 km of the core-collapsing massive star is followed from pre-bounce to post-bounce. Unlike other groups (Janka & Müller 1996; Swesty & Myra 2005ab), for greater consistency we do not start the simulation at post-bounce times by remapping a 1D simulation evolved till core bounce. Second, the VULCAN/2D grid, by switching from Cartesian (cylindrical) in the inner region (roughly the central 100 km²) to spherical above a few tens of kilometers (chosen as desired), allows us to maintain good resolution, while preventing the Courant timestep from becoming prohibitively small. Unlike previous studies of PNS convection (e.g., Swesty & Myra 2005ab), we extend the grid right down to the center, without the excision of the inner kilometers. Additionally, this grid naturally permits the core to move and, thus, in principle, provides a consistent means to assess the core recoil associated with asymmetric explosions. Third, the large radial extent of the simulation, from the inner core to a few thousand km, allows us to consider the feedback effects between different regions. Fourth, our use of Multi-Group Flux-Limited Diffusion is also particularly suited for the analysis of mechanisms occurring within a radius of 50 km, since there, neutrinos have a diffusive behavior, enforced by the high opacity of the medium at densities above 10^{11} g cm⁻³. Fifth, lateral transport of neutrino energy and lepton number is accounted for explicitly, an asset over the more approximate ray-by-ray approach (Burrows, Hayes, & Fryxell 1995; Buras et al. 2005) which cannot simulate accurately the behavior of doubly-diffusive instabilities. A limitation of our work is the neglect of the subdominant inelastic $e^- - \nu_e$ scattering in this version of VULCAN/2D.

The present paper is structured as follows. In §2, we discuss the VULCAN/2D code on which all simulations studied here are based. In §3, we describe in detail the properties of our baseline model simulation, emphasizing the presence/absence of convection, and limiting the discussion to the inner 50-100 km. In §4, focusing on results from our baseline model, we characterize the PNS convection and report the lack of doubly-diffusive instabilities within the PNS. Additionally, we report the unambiguous presence of gravity waves, persisting over a few hundred milliseconds, close to the minimum in the electron-fraction distribution, at ~ 20 -30 km. In §5, we conclude and discuss the broader significance of our results in the context of the mechanism of core-collapse supernovae.

2. VULCAN/2D AND SIMULATION CHARACTERISTICS

All radiation-hydrodynamics simulations presented in this paper were performed with a time-explicit variant of VULCAN/2D (Livne 1993), adapted to model the mechanism of core-collapse supernovae (Livne et al. 2004; Walder et al. 2005; Ott et al. 2004). The code uses cylindrical coordinates (r, z) where z is the distance parallel to the axis of symmetry (and, sometimes, the axis

of rotation) and r is the position perpendicular to it ⁴. VULCAN/2D has the ability to switch from a Cartesian grid near the base to a spherical-polar grid above a specified transition radius R_t . A reasonable choice is $R_t \sim 20$ km since it allows a moderate and quite uniform resolution of both the inner and the outer regions, with a reasonably small total number of zones that extends out to a few thousand kilometers. With this setup, the “horns,”⁵ associated with the Cartesian-to-spherical-polar transition, lie in the region where PNS convection obtains and act as (additional) seeds for PNS convection (see below). We have experimented with alternate grid setups that place the horns either interior or exterior to the region where PNS convection typically obtains, i.e., roughly between 10–30 km (Keil et al. 1996; Buras et al. 2005). We have performed three runs covering from 200 ms before to ~ 300 ms after core bounce, using 25, 31, and 51 zones out to the transition radius at 10, 30, and 80 km, placing the horns at 7, 26, and 65 km, respectively. Outside of the Cartesian mesh, we employ 101, 121, and 141 angular zones, equally spaced over 180° , and allocate 141, 162, and 121 logarithmically-spaced zones between the transition radius and the outer radius at 3000, 3800, and 3000 km, respectively. The model with the transition radius at 30 km modifies somewhat the timing of the appearance of PNS convection; the model with the transition radius at 80 km is of low resolution and could not capture the convective patterns in the inner grid regions. In this work, we thus report results for the model with the transition radius at 10 km, which possesses a smooth grid structure in the region where PNS convection obtains and a very high resolution of 0.25 km within the transition radius, but has the disadvantage that it causes the Courant timestep to typically be a third of its value in our standard computations (e.g. Burrows et al. 2006), i.e., $\sim 3 \times 10^{-7}$ s.

As mentioned in §1, this flexible grid possesses two assets: the grid resolution is essentially uniform everywhere interior to the transition radius, and, thus, does not impose a prohibitively small Courant timestep for our explicit hydrodynamic scheme, and the motion of the core is readily permitted, allowing estimates of potential core recoils resulting from global asymmetries in the fluid/neutrino momentum. The inner PNS can be studied right down to the core of the objects since no artificial inner (reflecting) boundary is placed there (Burrows, Hayes, & Fryxell 1995; Janka & Müller 1996; Keil, Janka & Müller 1996; Swesty & Myra 2005ab). Along the axis, we use a reflecting boundary, while at the outer grid radius, we prevent any flow of material ($V_R = 0$), but allow the free-streaming of the neutrinos.

We simulate neutrino transport using a diffusion approximation in 2D, together with a 2D version of Bruenn’s (1985) 1D flux limiter; some details of our approach and the numerical implementation in VULCAN/2D are presented in Appendix A. To improve over previous gray transport schemes, we solve the transport at different neutrino energies using a coarse, but satisfactory, sampling at 16 energy groups equally spaced in the log between 1 and 200 MeV. We have also investigated

the consequences of using a lower energy resolution, with only 8 energy groups, and for the PNS region we find no differences of a qualitative nature, and, surprisingly, few differences of a quantitative nature. While the neutrino energy distribution far above the neutrinosphere(s) (few 1000 km) has a thermal-like shape with a peak at ~ 15 MeV and width of ~ 10 MeV, deep in the nascent PNS, the distribution peaks beyond 100 MeV and is very broad. In other words, we use a wide range of neutrino energies to solve the transport in order to model absorption/scattering/emission relevant at the low energies exterior to the neutrinospheres, and at the high energies interior to the neutrinospheres.

We employ the equation of state (EOS) of Shen et al. (1998), since it correctly incorporates alpha particles and is more easily extended to lower densities and higher entropies than the standard Lattimer & Swesty (1991) EOS. We interpolate in 180 logarithmically-spaced points in density, 180 logarithmically-spaced points in temperature, and 50 linearly-spaced points in electron fraction, whose limits are $\{\rho_{\min}, \rho_{\max}\} = \{10^5, 10^{15}\}$ (g cm^{-3}), $\{T_{\min}, T_{\max}\} = \{0.1, 40\}$ (MeV), and $\{Y_{e,\min}, Y_{e,\max}\} = \{0.05, 0.513\}$.

The instabilities that develop in the early stages of the post-bounce phase are seeded by noise at the part in $\sim 10^6$ level in the EOS table interpolation. Beyond these, we introduce no artificial numerical perturbations. The “horns” associated with the Cartesian-to-spherical-polar transition are sites of artificially enhanced vorticity/divergence, with velocity magnitudes systematically larger by a few tens of percent compared to adjacent regions. In the baseline model with the transition radius at 10 km, this PNS convection sets in ~ 100 ms after core bounce, while in the simulation with the transition radius (horns) at 30 km (26 km), it appears already quite developed only ~ 50 ms after core bounce. In that model, the electron-fraction distribution is also somewhat “squared” interior to 20 km, an effect we associate with the position of the horns, not present in either of the alternate grid setups. Thus, the Cartesian-to-spherical-polar transition introduces artificial seeds for PNS convection, although such differences are of only a quantitative nature. The most converged results are, thus, obtained with our baseline model, on which we focus in the present work. For completeness, we present, in Figs. 2–4, a sequence of stills depicting the pre-bounce evolution of our baseline model.

In this investigation, we employ a single progenitor model, the $11 M_\odot$ ZAMS model (s11) of Woosley & Weaver (1995); when mapped onto our Eulerian grid, at the start of the simulation, the $1.33 M_\odot$ Fe-core, which stretches out to 1300 km, is already infalling. Hence, even at the start of the simulation, the electron fraction extends from 0.5 above the Fe core down to 0.43 at the center of the object.

Besides exploring the dependence on PNS convection of the number of energy groups, we have also investigated the effects of rotation. For a model with an initial inner rotational period of 10.47 seconds ($\Omega = 0.6 \text{ rad s}^{-1}$), taken from Walder et al. (2005), and with a PNS spin period of 10 ms after ~ 200 ms (Ott et al. 2005), we see no substantive differences with our baseline model. Hence, we have focused in this paper on the results from the

⁴ The spherical radius, R , is given by the quantity $\sqrt{r^2 + z^2}$.

⁵ For a display of the grid morphology, see Fig. 4 in Ott et al. (2004).

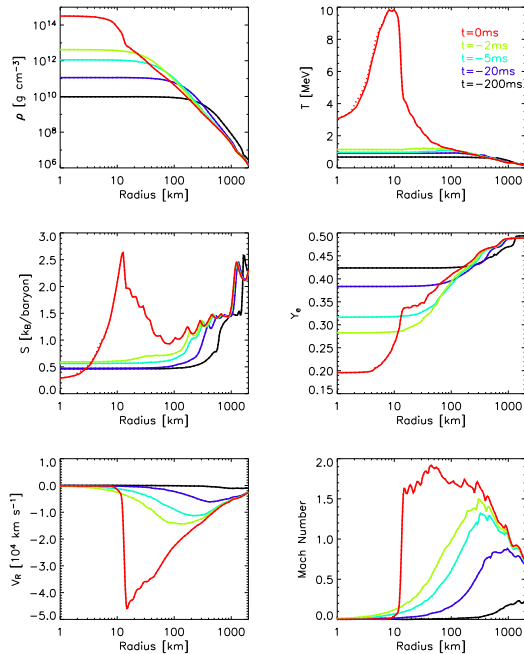


FIG. 1.— Montage of radial cuts along the polar (90° ; solid line) and equatorial (dotted line) direction at 200 (black), 20 (blue), 5 (cyan), 2 (green), and 0 ms (red) before core bounce for the density (top left), temperature (top right), entropy (middle left), Y_e (middle right), radial velocity (bottom left), and Mach number (bottom right).

non-rotating baseline model ⁶.

Finally, before discussing the results for the baseline model, we emphasize that the word “PNS” is to be interpreted loosely: we mean by this the regions of the simulated domain that are within a radius of ~ 50 km. If the explosion fails, the entire progenitor mantle will eventually infall and contribute its mass to the compact object. If the explosion succeeds, it remains to be seen how much material will reach escape velocities. At 300 ms past core bounce, about 95% of the progenitor core mass is within 30 km.

3. DESCRIPTION OF THE RESULTS OF THE BASELINE MODEL

In this section, we present results from the baseline VULCAN/2D simulation, whose parameters and characteristics were described in §2. First, we present for the pre-bounce phase a montage of radial slices of the density (top-left), electron-fraction (top-right), temperature (middle-left), entropy (middle-right), radial-velocity (bottom-left), and Mach number (bottom right) in Fig. 1, using a solid line to represent the polar direction (90°) and a dotted-line for the equatorial direction. All curves overlap to within a line thickness, apart from the red curve, which corresponds to the bounce-phase (within 1 ms after bounce), showing the expected and trivial result that the collapse is indeed purely spherical.

Now, let us describe the gross properties of the simulation, covering the first 300 ms past core bounce and focusing exclusively on the inner ~ 50 km. In Figs. 2–

4, we show stills of the entropy (Fig. 2), electron fraction (Fig. 3), and density (Fig. 4) at 50 (top left panel), 100 (top right), 200 (bottom left), and 300 ms (bottom right) after core bounce. We also provide, in Fig. 5, radial cuts of a sample of quantities in the equatorial direction, to provide a clearer view of, for example, gradients. Overall, the velocity magnitude is in excess of 4000 km s^{-1} only beyond ~ 50 km, while it is systematically below 2000 km s^{-1} within the same radius. At early times after bounce ($t = 50$ ms), the various plotted quantities are relatively similar throughout the inner 50 km. The material velocities are mostly radial, oriented inward, and very small, *i.e.*, do not exceed $\sim 1000 \text{ km s}^{-1}$. The corresponding Mach numbers throughout the PNS are subsonic, not reaching more than $\sim 10\%$ of the local sound speed. This rather quiescent structure is an artefact of the early history of the young PNS before vigorous dynamics ensues. The shock wave generated at core bounce, after the initial dramatic compression up to nuclear densities ($\sim 3 \times 10^{14} \text{ g cm}^{-3}$) of the inner progenitor regions, leaves a positive entropy gradient, reaching then its maximum of $\sim 6\text{--}7 \text{ k}_B/\text{baryon}$ at ~ 150 km, just below the shock. The electron fraction (Y_e) shows a broad minimum between ~ 30 and ~ 90 km, a result of the continuous deleptonization of the corresponding regions starting after the neutrino burst near core bounce. Within the innermost radii ($\sim 10\text{--}20$ km), the very high densities ($\geq 10^{12} \text{ g cm}^{-3}$) ensure that the region is optically-thick to neutrinos, inhibiting their escape.

Turning to the next phase in our time series ($t = 100$ ms), we now clearly identify four zones within the inner 50 km, ordered from innermost to outermost, which will become increasingly distinct with time:

- Region A: This is the innermost region, within 10 km, with an entropy of $\sim 1 \text{ k}_B/\text{baryon}$, a Y_e of 0.2–0.3, a density of $\sim 1\text{--}4 \times 10^{14} \text{ g cm}^{-3}$, essentially at rest with a near-zero Mach number (negligible vorticity and divergence). This region has not appreciably changed in the elapsed 50 ms, and will in fact not do so for the entire evolution described here.
- Region B: Between 10 and 30 km, we see a region of higher entropy ($2\text{--}5 \text{ k}_B/\text{baryon}$) with positive-gradient and lower Y_e with negative gradient (from Y_e of ~ 0.3 down to ~ 0.1). Despite generally low Mach number, this region exhibits significant motions with pronounced vorticity, resulting from the unstable negative-gradient of the electron (lepton) fraction.
- Region C: Between 30 and 50 km is a region of outwardly-increasing entropy ($5\text{--}8 \text{ k}_B/\text{baryon}$), but with a flat and low electron fraction; this is the most deleptonized region in the entire simulated object at this time. There, velocities are vanishingly small ($\ll 1000 \text{ km s}^{-1}$), as in Region A, although generally oriented radially inwards. This is the cavity region where gravity waves are generated, most clearly at 200–300 ms in our time series.
- Region D: Above 50 km, the entropy is still increasing outward, with values in excess of $8 \text{ k}_B/\text{baryon}$, but now with an outwardly-increasing Y_e (from the

⁶ The consequences in the PNS core of much faster rotation rates will be the subject of a future paper.

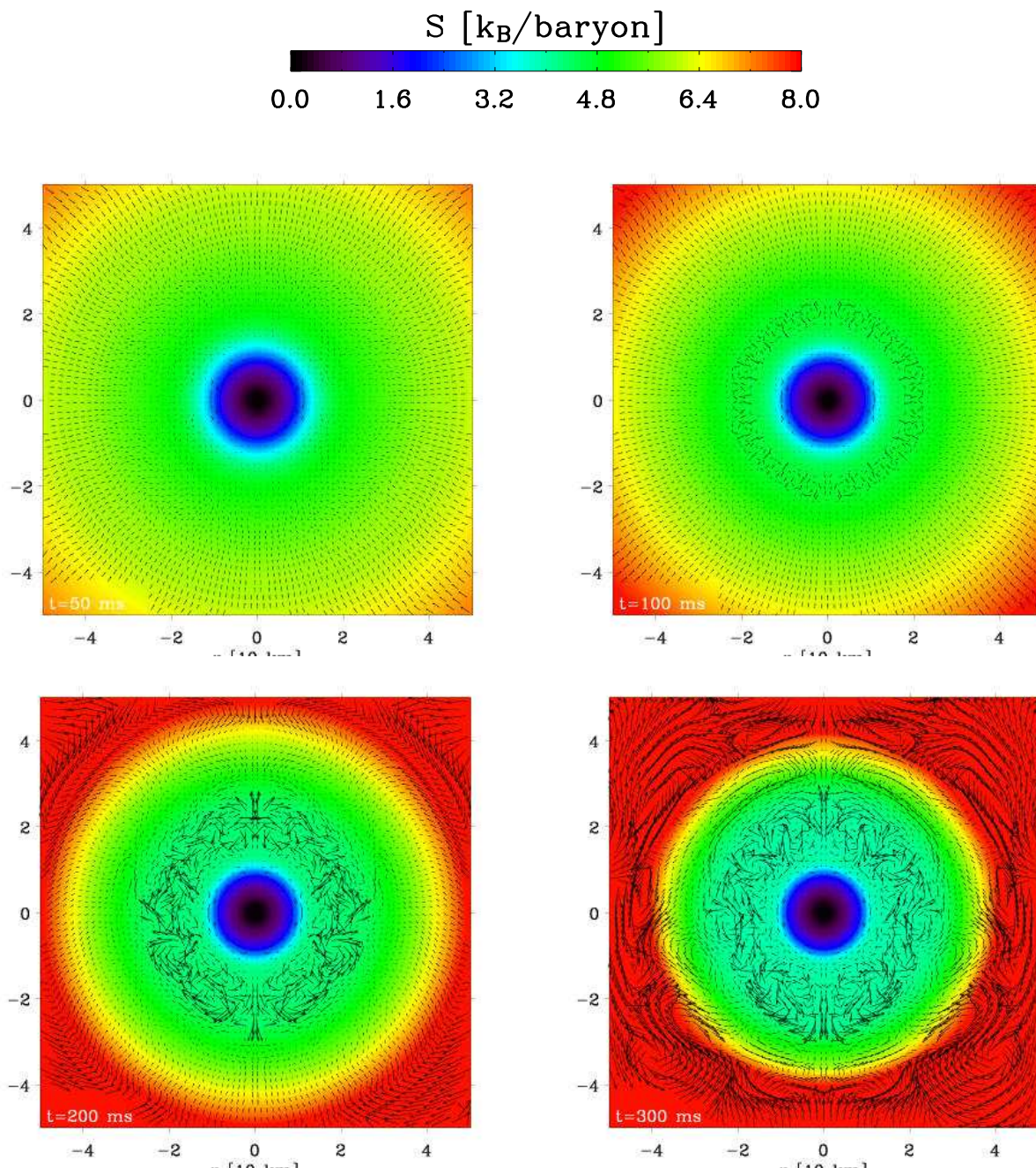


FIG. 2.— Color map stills of the entropy, taken at 50 (top left), 100 (top right), 200 (bottom left), and 300 ms (bottom right) past core bounce, with velocity vectors overplotted. Here “Width” refers to the diameter; the radius through the middle is 50 kilometers. Note that to ease the comparison between panels, the same range of values of the color map are used throughout (see text for discussion). In all panels, the length of velocity vectors is saturated at 2000 km s^{-1} , a value only reached in the bottom-row panels. Note that the assessment of velocity magnitudes is best done using Fig. 5 and Figs. 7-8 (see text for discussion).

minimum of 0.1 up to 0.2). Velocities are much larger than those seen in Region B, although still corresponding to subsonic motions at early times. Negligible vorticity is generated at the interface between Regions C and D. The radially infalling material is prevented from entering Region C and instead settles on its periphery.

As time progresses, these four regions persist, evolving only slowly for the entire ~ 300 ms after bounce. The electron fraction at the outer edge of Region A decreases. The convective motions in low- Y_e Region B induce significant mixing of the high- Y_e interface with Region A, smoothing the Y_e peak at ~ 10 km. Overall, Region A is the least changing region. In Region B, convective mo-

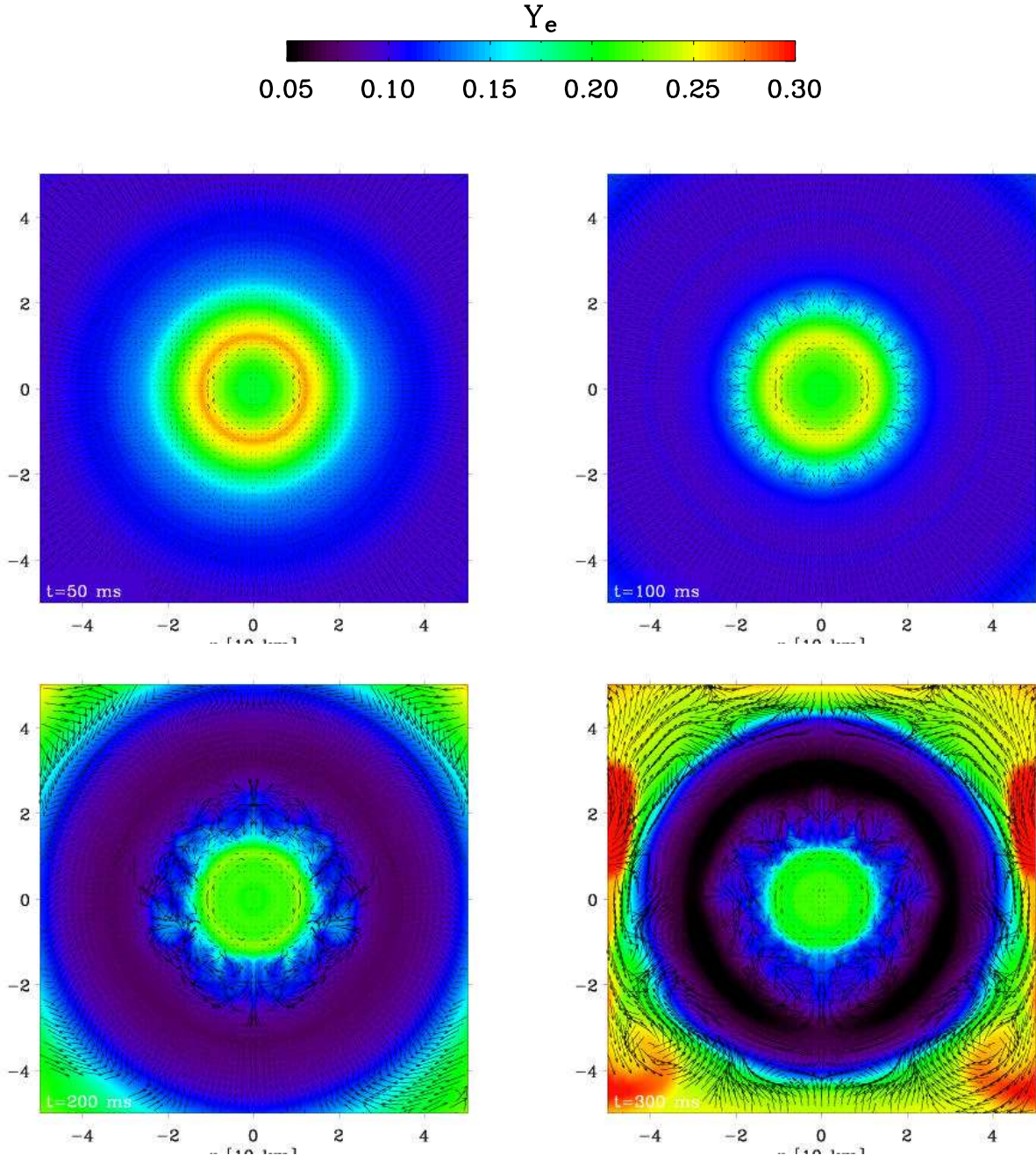


FIG. 3.— Same as Fig. 2, but for the electron fraction Y_e . (See text for discussion.)

tions, although subsonic, are becoming more violent with time, reaching Mach numbers of ~ 0.1 at 200–300 ms, associated with a complex flow velocity pattern. In Region C, the trough in electron fraction becomes more pronounced, reaching down to 0.1 at 200 ms, and a record-low of 0.05 at 300 ms. Just on its outer edge, one sees sizable (a few $\times 100 \text{ km s}^{-1}$) and nearly-exclusively latitudinal motions, persisting over large angular scales. Region D has changed significantly, displaying low-density, large-scale structures with downward and upward velocities. These effectively couple remote regions, between

the high-entropy, high- Y_e shocked region and the low-entropy, low- Y_e Region C. Region D also stretches further in (down to $\sim 45 \text{ km}$), at the expense of Region C which becomes more compressed. This buffer region C seems to shelter the interior, which has changed more modestly than region D.

Figure 5 shows radial cuts along the equator for the four time snapshots (black: 50 ms; blue: 100 ms; green: 200 ms; red: 300 ms) shown in Figs. 2–4 for the density (upper left), temperature (upper right), entropy (middle left), Y_e (middle right), radial velocity (bottom left),

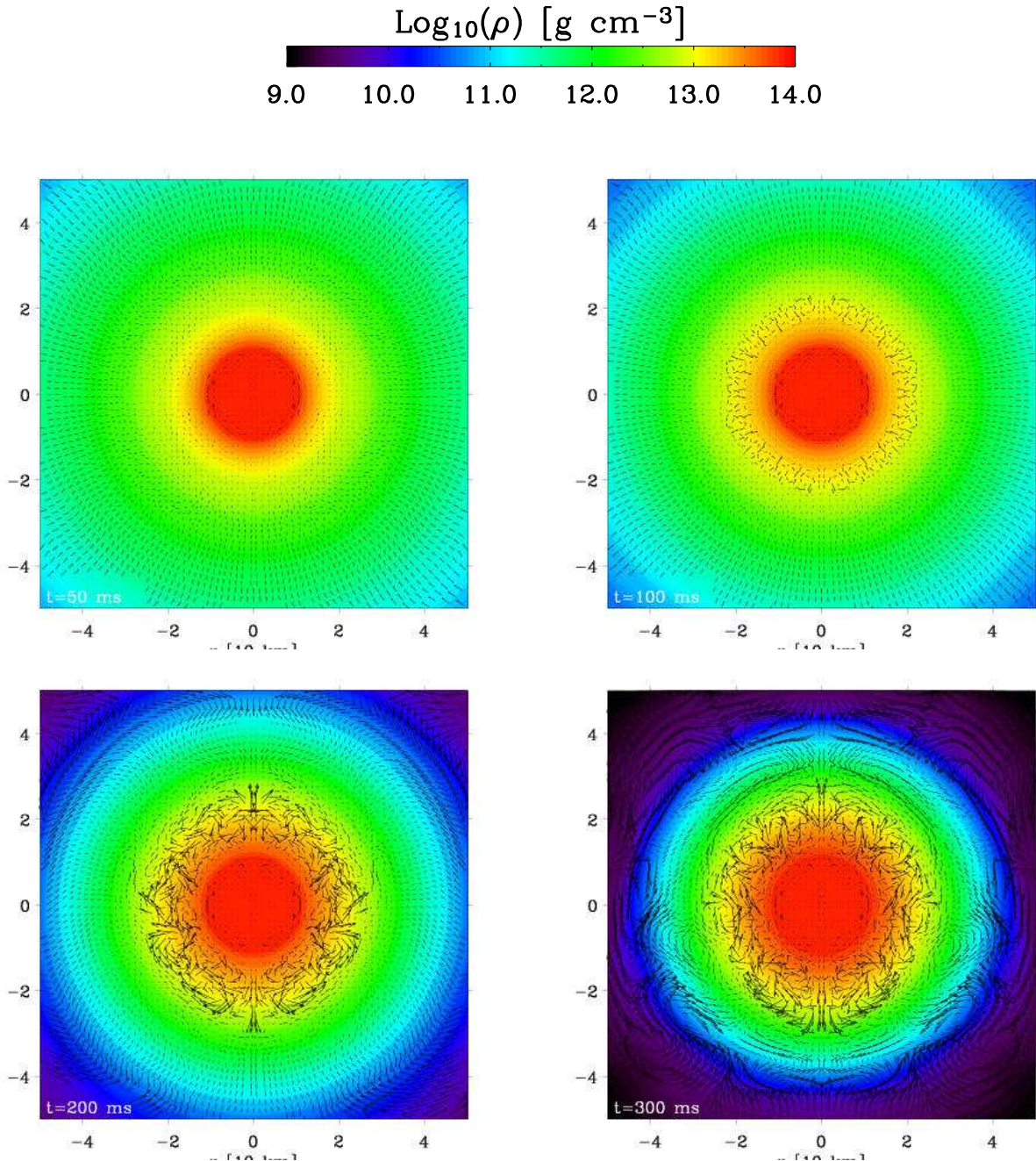


FIG. 4.— Same as Fig. 2, but for the mass density ρ . (See text for discussion.)

and Mach number (bottom right). Notice how the different regions are clearly visible in the radial-velocity plot, showing regions of significant upward/downward motion around 20 km (Region B) and above ~ 50 km (Region D). One can also clearly identify the Y_e trough, whose extent decreases from 30–90 km at 50 ms to 30–40 km at 300 ms. The below-unity Mach number throughout the inner 50 km also argues for little ram pressure associated with convective motions in those inner regions. Together with the nearly-zero radial velocities in Regions A and C at all times, this suggests that of these three regions

mass motions are confined to Region B.

One can identify a trend of systematic compression of Regions B–C–D, following the infall of the progenitor mantle. Indeed, despite the near-stationarity of the shock at 100–200 km over the first 200–300 ms, a large amount of mass flows inward through it, coming to rest at smaller radii. In Fig. 6, we display the evolution, up to 300 ms past core bounce, of the interior mass and mass flow through different radial shells within the PNS. Note that mass inflow in this context has two components: 1) direct accretion of material from the infalling progenitor

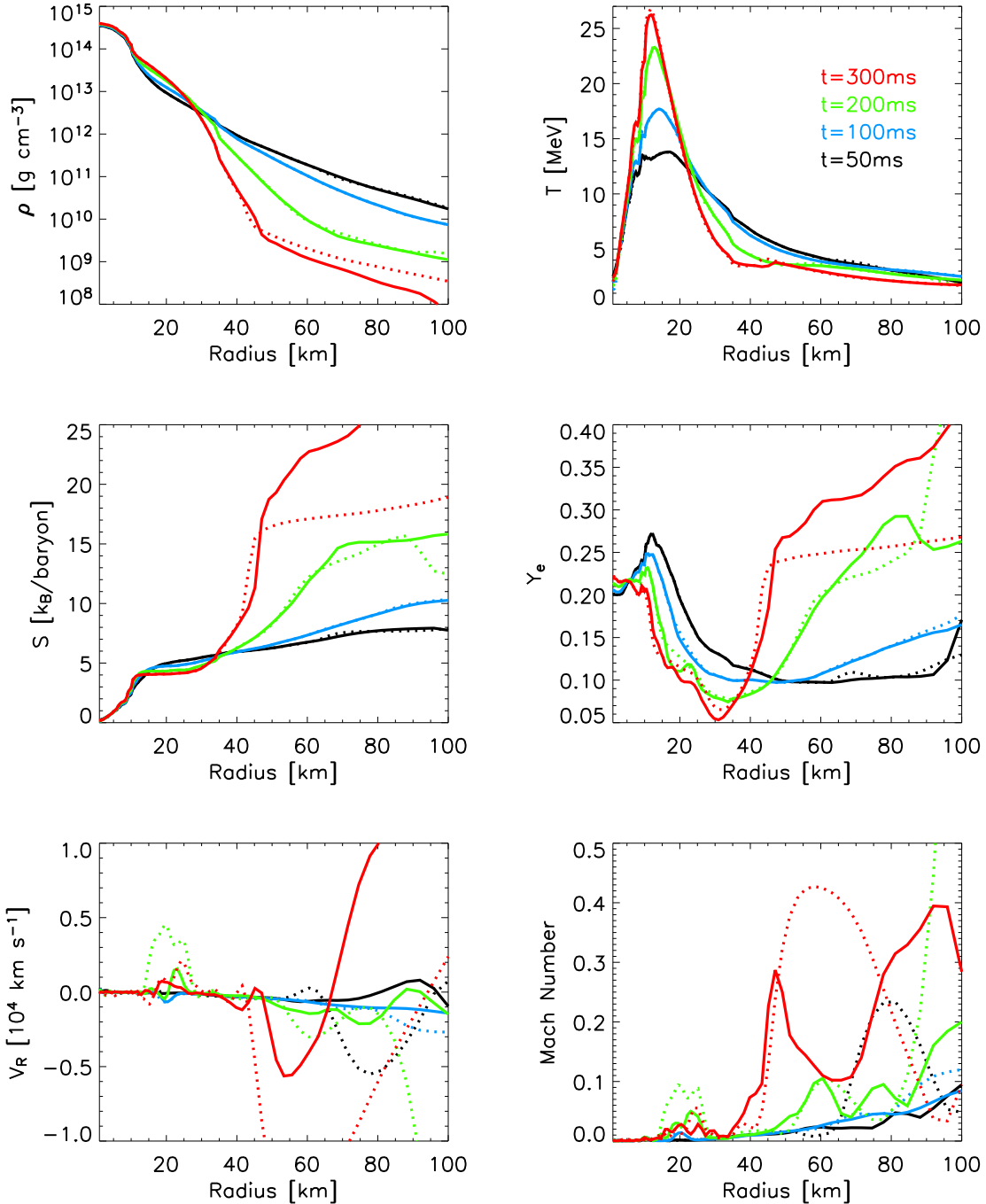


FIG. 5.— Montage of radial cuts along the equatorial direction at 50 (black), 100 (blue), 200 (green), and 300 ms (red) past core bounce, echoing the properties displayed in Figs 2-4 for the baseline model, for the density (top left), temperature (top right), entropy (middle left), Y_e (middle right), radial velocity (bottom left), and Mach number (bottom right).

envelope and, 2) the compression of the PNS material as it cools and deleptonizes. Hence, mass inflow through radial shells within the PNS would still be observed even in the absence of explicit accretion of material from the shock region. By 300 ms past core bounce, the “accretion rate” has decreased from a maximum of $\sim 1\text{--}3 M_\odot \text{ s}^{-1}$ at 50 ms down to values below $0.1 M_\odot \text{ s}^{-1}$ and the interior mass at 30 km has reached up to $\sim 1.36 M_\odot$, i.e., 95% of the progenitor core mass. Interestingly, the mass flux at

a radius of 20 km is lower (higher) at early (late) times compared to that in the above layers, and remains non-negligible even at 300 ms.

An instructive way to characterize the properties of the fluid within the PNS is by means of Distribution Functions (DFs), often employed for the description of the solar convection zone (Browning, Brun, & Toomre 2004). Given a variable x and a function $f(x)$, one can compute, for a range of values y encompassing the extrema

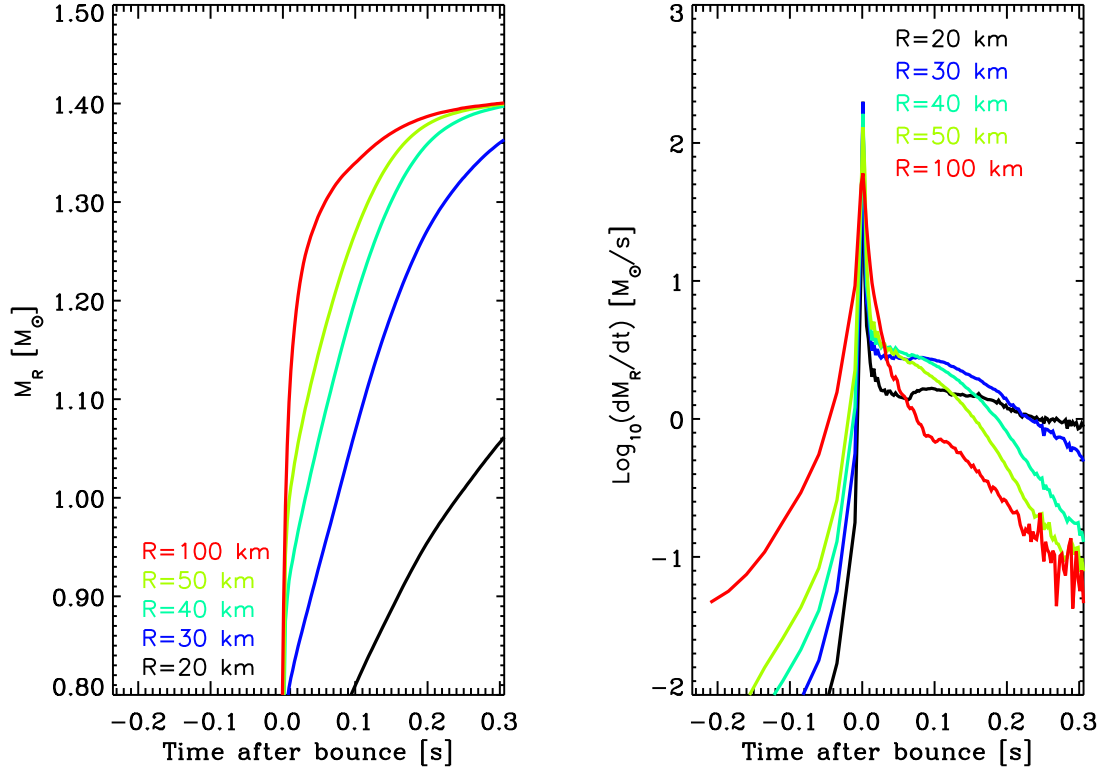


FIG. 6.— *Left*: Time evolution after bounce of the interior mass spherical shells at selected radii: 20 km (black), 30 km (blue), 40 km (red) and 50 km (black). *Right*: Corresponding mass flow through the same set of radii.

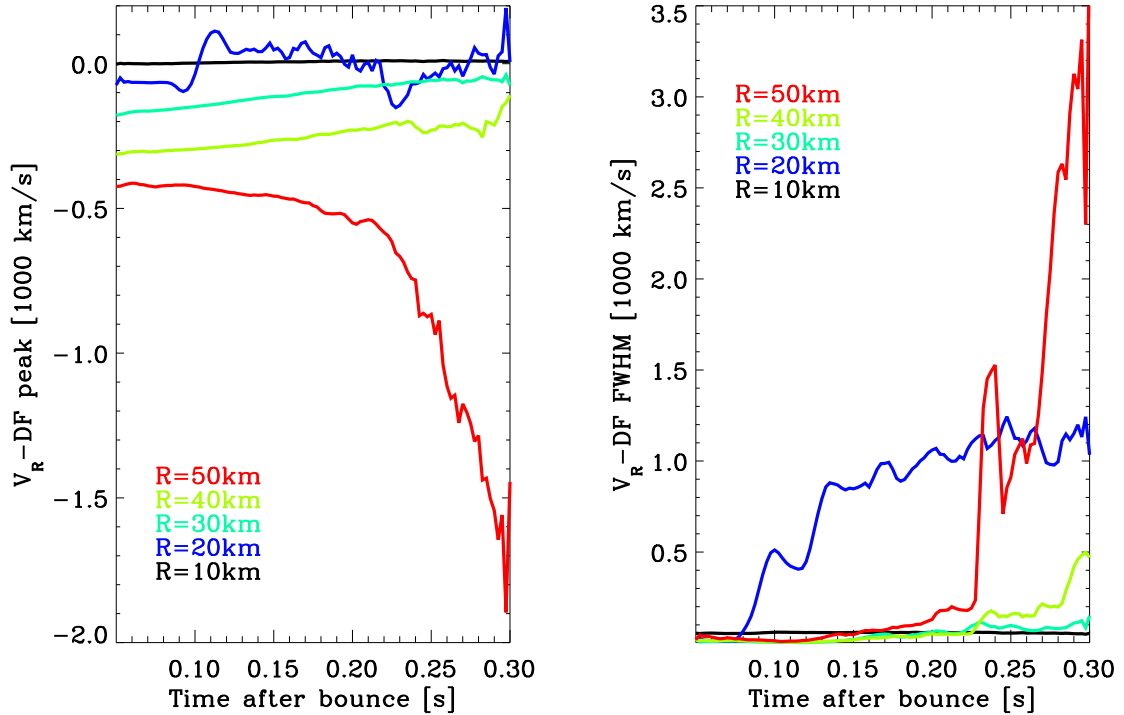


FIG. 7.— Time evolution, at selected radii, of the radial-velocity at peak and Full Width at Half Maximum (FWHM) of the radial-velocity distribution function. (See text for discussion.)

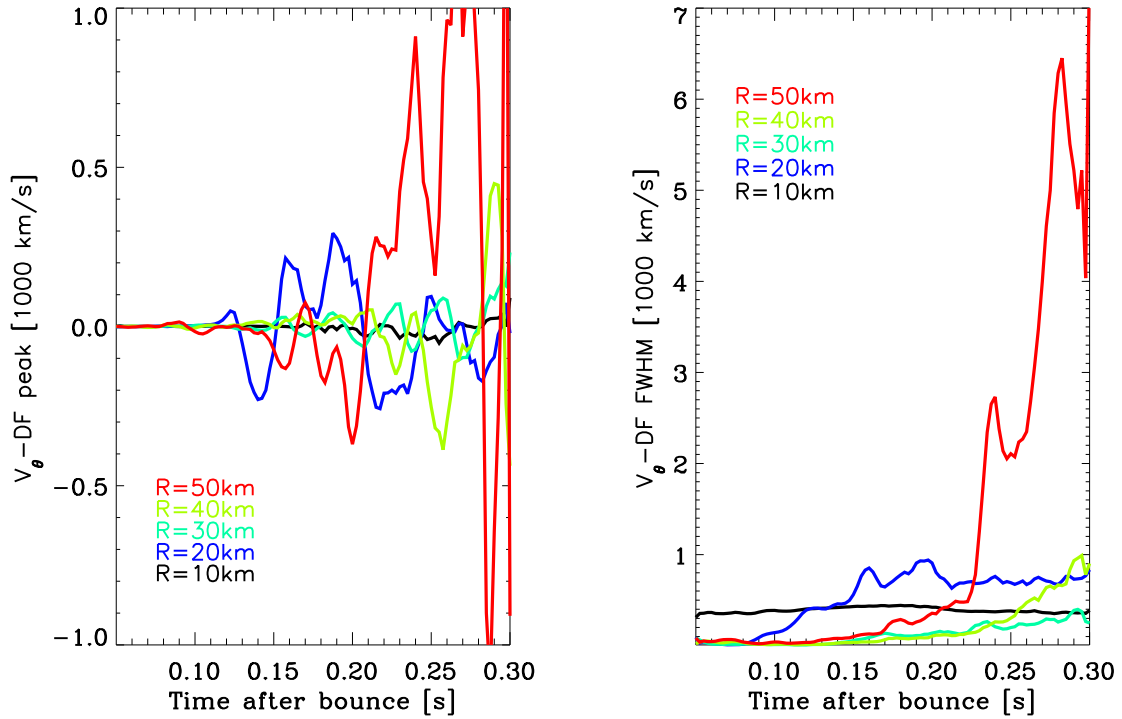


FIG. 8.— Same as Fig. 7, but for the latitudinal velocity, V_{θ} .

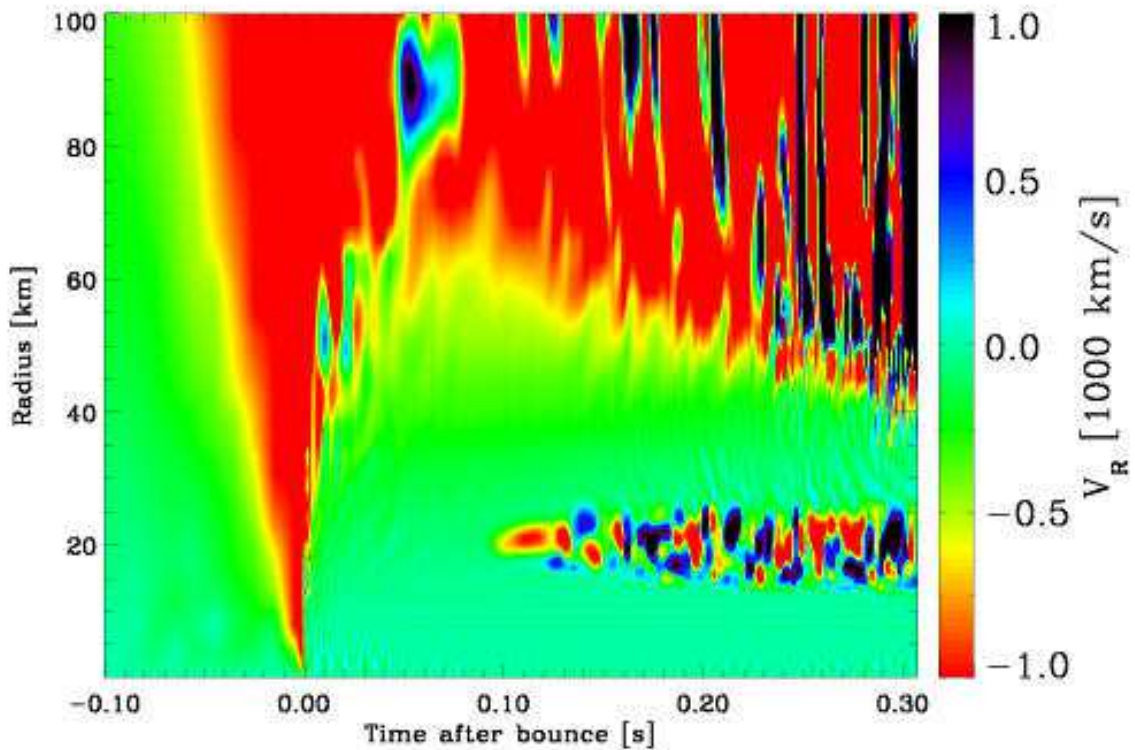


FIG. 9.— Color map of the radial velocity V_R as a function of time after bounce and radius, along the equatorial direction. The green regions denote relatively quiescent areas. The inner region of the outer convective zone (Region D) is the predominately red zone; the horizontal band near ~ 20 km is Region B, where isolated PNS convection obtains. See Buras et al. (2005) for a similar plot and the text for details.

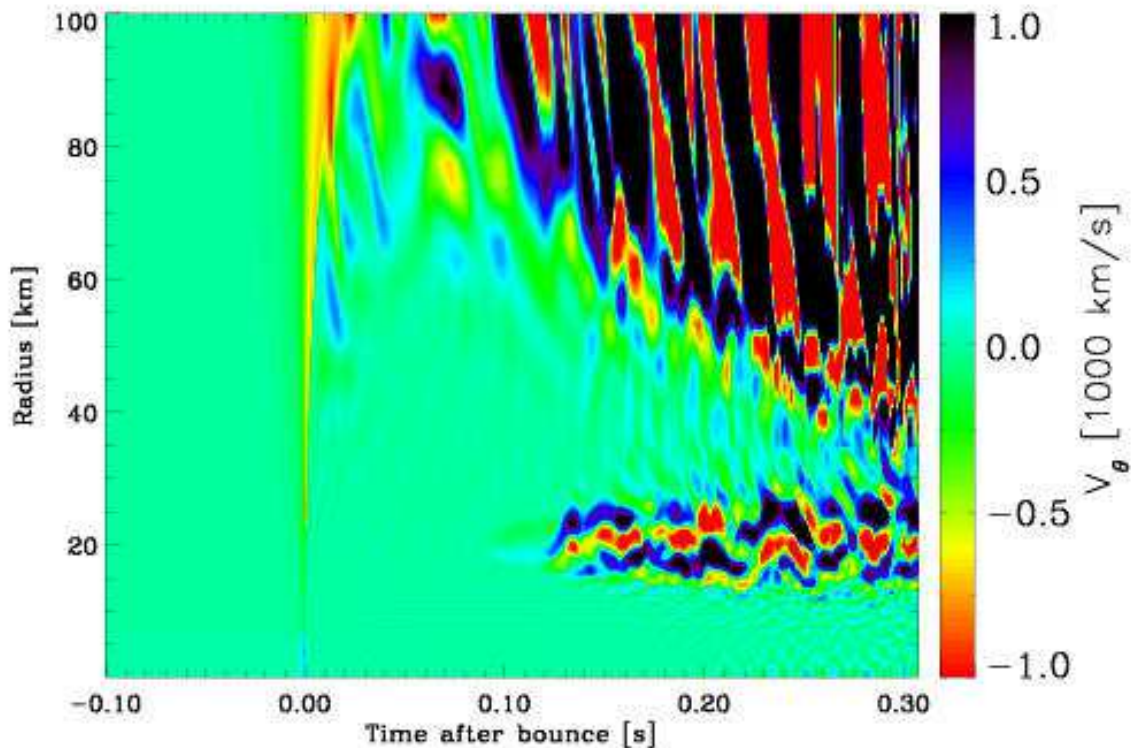


FIG. 10.— Same as Fig. 9, but for the latitudinal velocity (V_θ). Note the gravity waves excited between 30–40 km, more visible in this image of the latitudinal velocity than in the previous figure for the radial velocity.

of $f(x)$, the new function

$$g(f(x), y) \propto \exp \left[- \left(\frac{y - f(x)}{\sqrt{2}\sigma} \right)^2 \right],$$

where $\sigma = \sqrt{\langle f^2(x) \rangle_x - \langle f(x) \rangle_x^2}$ and $\langle \rangle_x$ is to be understood as an average over x . We then construct the new function:

$$h(y) = \langle g(f(x), y) \rangle_x.$$

Here, to highlight the key characteristics of various fluid quantities, we extract only the y value y_{peak} at which $h(y)$ is maximum, *i.e.*, the most representative value $f(x)$ in our sample over all x (akin to the mean), and the typical scatter around that value, which we associate with the Full Width at Half Maximum (FWHM) of the Gaussian-like distribution.

In Figs. 7-8 and 11-12, we plot such peak and FWHM values at selected radii within the PNS, each lying in one of the Regions A, B, C, or D, covering the times between 50 and 300 ms after core bounce. Figure 7 shows the radial-velocity at the peak (left panel) and FWHM (right panel) of the radial-velocity distribution function. The black, blue, turquoise, and green curves (corresponding to radii interior to 40 km) are similar, being close to zero for both the peak and the FWHM. In contrast, the red curve (corresponding to a radius of 50 km) shows a DF with a strongly negative peak radial velocity, even more so at later times, while the FWHM follows the same evolution (but at positive values). This is in conformity

with the previous discussion. Above ~ 40 km (Region D), convection underneath the shocked region induces large-scale upward and downward motions, with velocities of a few 1000 km s^{-1} , but negative on average, reflecting the continuous collapse of the progenitor mantle (Fig. 6). Below ~ 40 km, there is no sizable radial flow of material biased towards inflow, on average or at any time. This region is indeed quite dynamically decoupled from the above regions during the first ~ 300 ms, in no obvious way influenced by the fierce convection taking place underneath the shocked region. Turning to the distribution function of the latitudinal velocity (Fig. 8), we see a similar dichotomy between its peak and FWHM at radii below and above 40 km. At each radius, V_θ is of comparable magnitude to V_R , apart from the peak value which remains close to zero even at larger radii (up to 40 km). This makes sense, since no body-force operates continuously pole-ward or equator-ward - the gravitational acceleration acts mostly radially. Radial- and latitudinal-velocity distribution functions are, therefore, strikingly similar at 10, 20, 30, and 40 km, throughout the first 300 ms after core bounce, quite unlike the above layer, where the Mach number eventually reaches close to unity between 50–100 km (Fig. 5). In these two figures, PNS convection is clearly visible at 20 km, with small peak, but very sizable FWHM, values for the velocity distributions, highlighting the large scatter in velocities at this height. Notice also the larger scatter of values for the lateral velocity at 10 km in Fig. 8, related to the presence of the horns and the transition radius at this

height.

In Figs. 9–10, we complement the previous two figures by showing the temporal evolution of the radial and latitudinal velocities, using a sampling of one millisecond, along the equatorial direction and over the inner 100 km. To enhance the contrast in the displayed properties, we cover the entire evolution computed with VULCAN/2D, from the start at 240 ms prior to, until 300 ms past core bounce. Note the sudden rise at ~ 0.03 s prior to bounce, stretching down to radii of ~ 2 –3 km, before the core reaches nuclear densities and bounces. The shock wave moves out to ~ 150 km (outside of the range shown), where it stalls. In the 50–100 km region along the equator, we observe mostly downward motions, which reflect the systematic infall of the progenitor envelope, but also the fact that upward motions (whose presence is inferred from the distribution function of the radial velocity) occur preferentially at non-zero latitudes. The minimum radius reached by these downward plumes decreases with time, from ~ 70 km at 100 ms down to ~ 40 km at 300 ms past core bounce. Note that these red and blue “stripes” are slanted systematically towards smaller heights for increasing time, giving corresponding velocities $\Delta r/\Delta t \sim -50$ km/10 ms ~ -5000 km s $^{-1}$, in agreement with values plotted in Fig. 5. The region of small radial infall above 30 km and extending to 60–35 km (from 50 to 300 ms past core bounce) is associated with the trough in the Y_e profile (Fig. 5), narrowing significantly as the envelope accumulates in the interior (Fig. 6). The region of alternating upward and downward motions around 20 km persists there at all times followed, confirming the general trend seen in Figs. 7–8. The inner 10 km (Region A) does not show any appreciable motions at any time, even with this very fine time sampling. The latitudinal velocity displays a similar pattern (Fig. 10) to that of the radial velocity, showing time-dependent patterns in the corresponding regions. However, we see clearly a distinctive pattern after 100 ms past bounce and above ~ 50 km, recurring periodically every ~ 15 ms. This timescale is comparable to the convective overturn time for downward/upward plumes moving back and forth between the top of Region C at ~ 50 km and the shock region at 150 km, with typical velocities of 5000 km s $^{-1}$, *i.e.* $\tau \sim 100$ km/ 5000 km s $^{-1} \sim 20$ ms. In Region C, at the interface between the two convective zones B and D, the latitudinal velocity V_θ has a larger amplitude and shows more time-dependence than the radial velocity V_R in the corresponding region. Interestingly, the periodicity of the patterns discernable in the V_θ field in Region C seems to be tuned to that in the convective Region D above, visually striking when one extends the slanted red and blue “stripes” from the convective Region D downwards to radii of ~ 30 km. This represents an alternative, albeit heuristic, demonstration of the potential excitation of gravity waves in Region C by the convection occurring above (see §4.3). What we depict in Figs. 9–10 is also seen in Fig. 29 of Buras et al. (2005), where, for their model s15Gio_32.b that switches from 2D to spherical-symmetry in the inner 2 km, PNS convection obtains ~ 50 ms after bounce and between 10–20 km. The similarity between the results in these two figures indicates that as far as PNS convection is concerned and besides differences in approaches, VULCAN/2D and MUDBATH compare well. Differences in the time of onset of PNS

convection may be traceable solely to differences in the initial seed perturbations, which are currently unknown. In MUDBATH, the initial seed perturbations are larger than those inherently present in our baseline run, leading to an earlier onset by ~ 50 ms of the PNS convection simulated by Buras et al. (2005).

We show the distribution function for the entropy in Fig. 11. Again, we see both in the entropy at the peak and the FWHM the dichotomy between the inner 30 km with low values, and the layers above, with much larger values for both. All radii within the PNS start, shortly after core bounce (here, the initial time is 50 ms), with similar values, around 5–7 k_B /baryon. Below 20 km, convective motions homogenize the entropy, giving the very low scatter, while the relative isolation of these regions from the convection and net neutrino energy deposition above maintains the peak value low. Outer regions (above 30 km) are considerably mixed with accreting material, enhancing the entropy considerably, up to values of 20–30 k_B /baryon.

To conclude this descriptive section, we show in Fig. 12 the distribution function for the electron fraction. The dichotomy reported above between different regions is present here. Above ~ 30 km, the Y_e increases with time as fresh material accretes from larger radii, while below this limit, the absent or modest accretion cannot compensate for the rapid electron capture and neutrino losses. Indeed, the minimum at 30 km and 300 ms corresponds roughly with the position of the neutrinosphere(s) at late times, which is then mostly independent of neutrino energy (§4).

4. PROTONEUTRON STAR CONVECTION, DOUBLY-DIFFUSIVE INSTABILITIES, AND GRAVITY WAVES

In this section, we connect the results obtained for our baseline model to a number of potential modes and instabilities that can arise within or just above the PNS (here again, we focus on the innermost 50–100 km), all related to the radial distribution of entropy and lepton number (or electron) fraction. Instead of a stable combination of negative entropy gradient and positive Y_e gradient in the PNS, the shock generated at core bounce leaves a positive entropy gradient in its wake, while the concomitant deleptonization due to neutrino losses at and above the neutrinosphere establishes a negative Y_e gradient. This configuration is unstable according to the Ledoux criterion and sets the background for our present discussion of PNS convection and motions.

4.1. Protoneutron Star Convection

In the preceding sections, we have identified two regions where sizable velocities persist over hundreds of milliseconds, associated with the intermediate Region B (covering the range 10–20 km) and the outer Region D considered here (above ~ 50 km). The latter is the region of advection-modified, neutrino-driven turbulent convection bounded by the shock wave. While this region does not directly participate in the PNS convection, it does influence the interface layer (Region C) and excites the gravity waves seen there (§4.3).

At intermediate radii (10–20 km, Region B), we have identified a region of strengthening velocity and vorticity, with little net radial velocity (≤ 100 km s $^{-1}$) at a

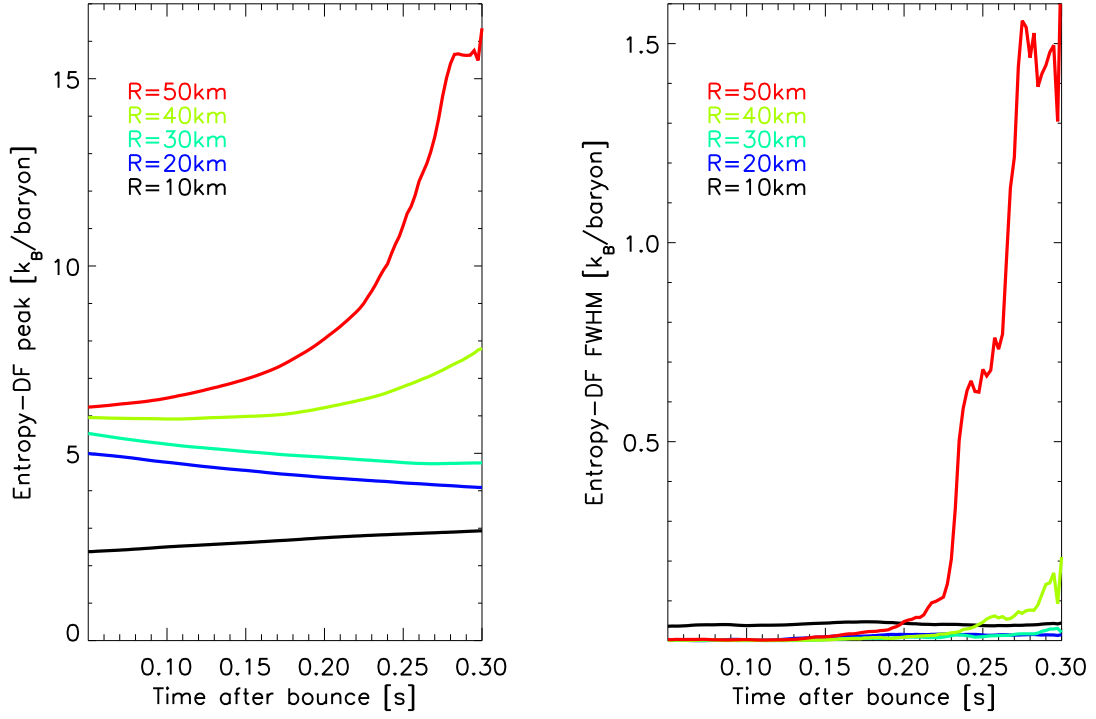


FIG. 11.— Time evolution after bounce, at selected radii, of the entropy at the peak (left) and FWHM (right) of the entropy distribution function.

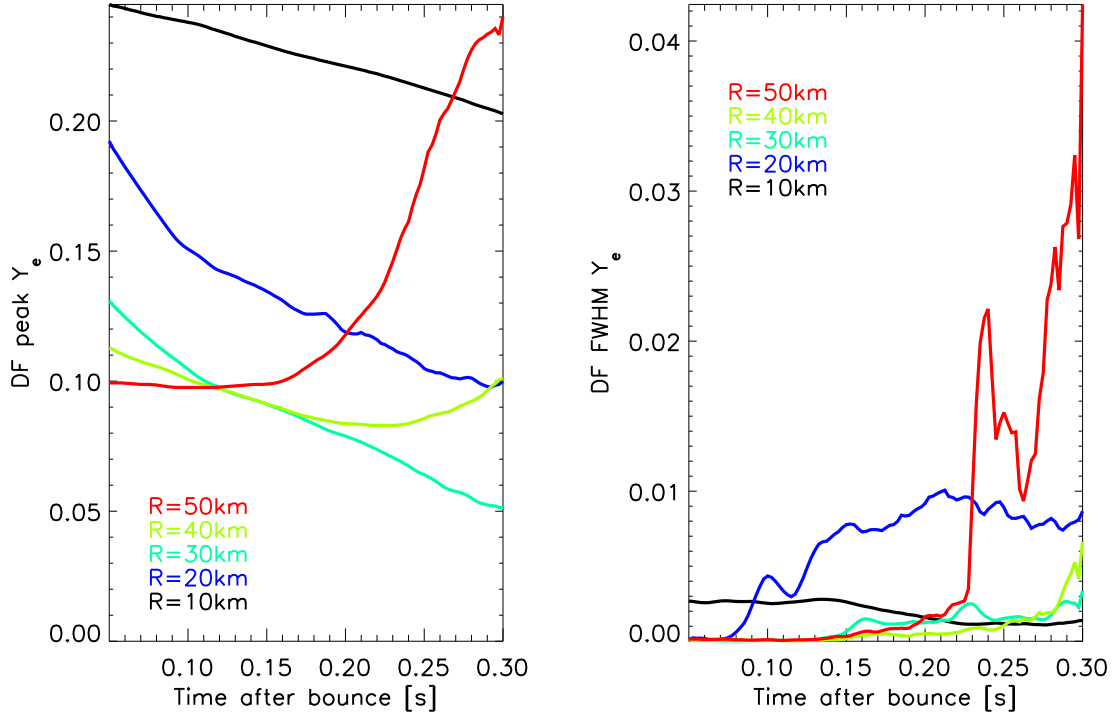


FIG. 12.— Same as Fig. 11, but for the electron fraction Y_e .

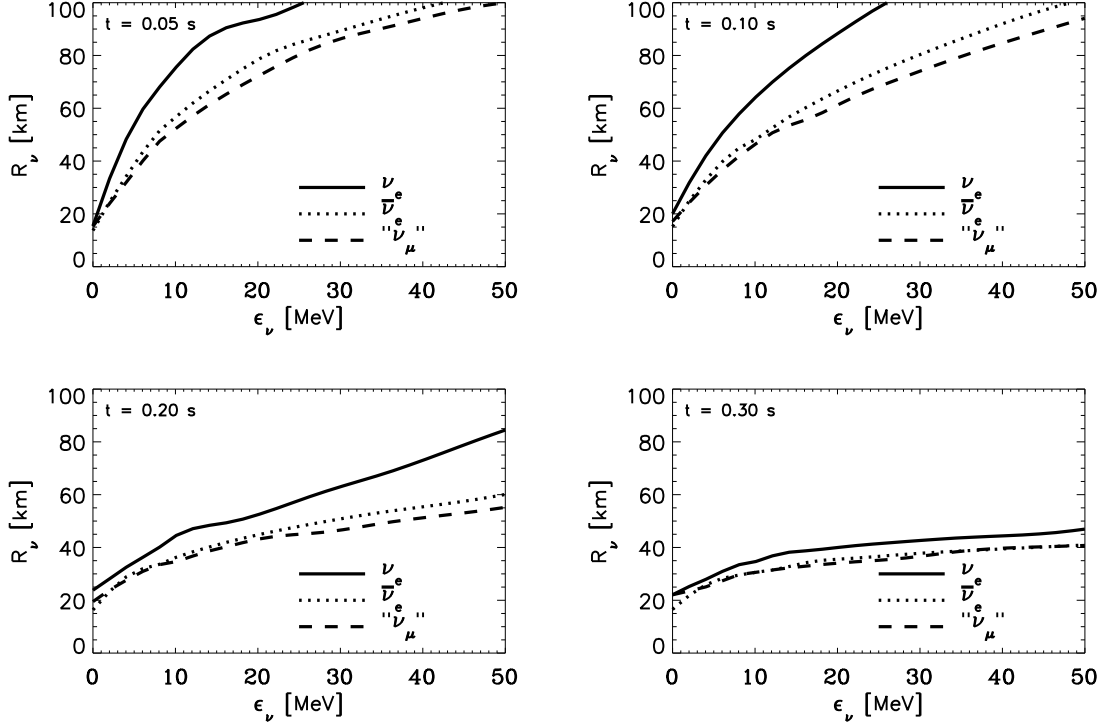


FIG. 13.— Neutrino energy dependence of neutrinosphere radii at four selected times past core bounce ($t = 50$ ms: top left; $t = 100$ ms: top right; $t = 200$ ms: bottom left; $t = 300$ ms: bottom right) for the three neutrino “flavors” (ν_e , solid line; $\bar{\nu}_e$, dotted line; ν_μ , dashed line) treated in our 16-energy-group baseline simulation.

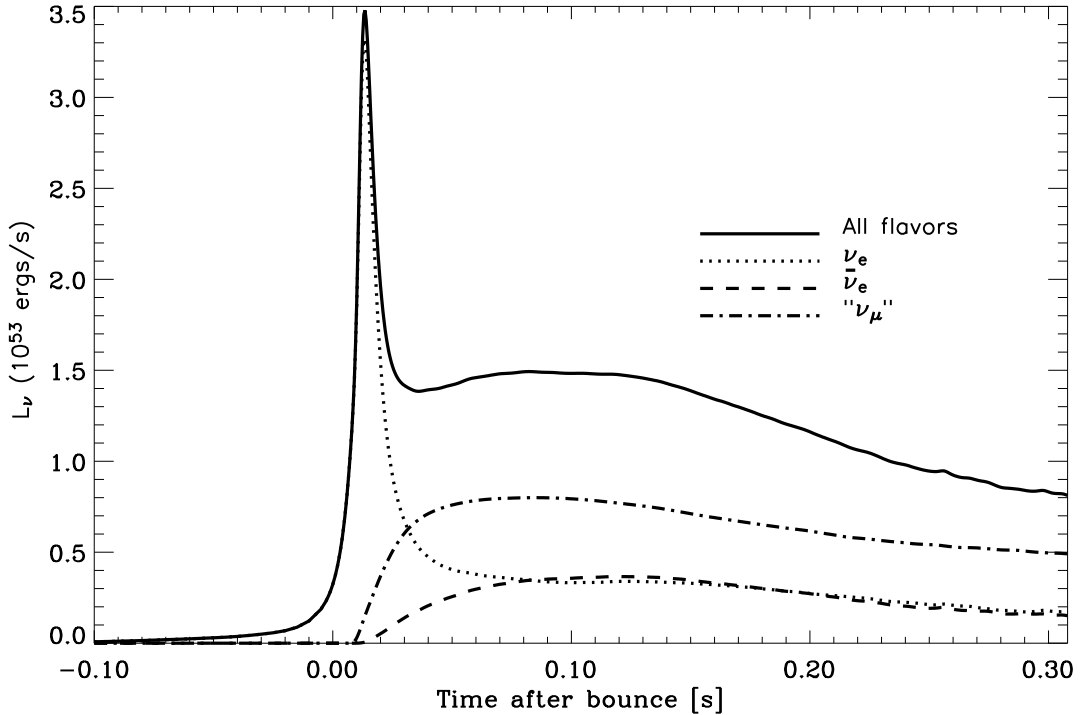


FIG. 14.— Time evolution of the neutrino luminosity, free-streaming through the outer grid radius at 3800 km, for the three neutrino “flavors” (ν_e , dotted line; $\bar{\nu}_e$, dashed line; ν_μ , dash-dotted line), as well as the sum of all three contributions (solid line), for our 16-energy-group baseline model. The time sampling is every 5 ms until $t = -6$ ms, and every 0.5 ms for the remaining of the simulation, where we have defined $t = 0$ as the time of hydrodynamical bounce.

given radius when averaged over all directions. In other words, significant motions are seen, but confined within a small region of modest radial extent of 10-20 km at most. As clearly shown in Fig. 5, this region has a rather flat entropy gradient, which cannot stabilize the steep negative $-Y_e$ gradient against this inner convection. This configuration is unstable according to the Ledoux criterion and had been invoked as a likely site of convection (Epstein 1979; Lattimer & Mazurek 1981; Burrows 1987). It has been argued that such convection, could lead to a sizable advection of neutrino energy upwards, into regions where neutrinos are decoupled from the matter (*i.e.*, with both low absorptive and scattering opacities), thereby making promptly available energy which would otherwise have diffused out over a much longer time.

The relevance of any advected flux in this context rests on whether the neutrino energy is advected from the diffusive to the free-streaming regions, *i.e.*, whether some material is indeed dredged from the dense and neutrino-opaque core out to and above the neutrinosphere(s). In Fig. 13, we show the energy-dependent neutrinospheric radii $R_\nu(\epsilon_\nu)$ at four selected times past core bounce (50, 100, 200, and 300 ms) for the three neutrino “flavors” (ν_e , solid line; $\bar{\nu}_e$, dotted line; “ ν_μ ”, dashed line), with $R_\nu(\epsilon_\nu)$ defined by the relation,

$$\tau(R_\nu(\epsilon_\nu)) = \int_{R_\nu(\epsilon_\nu)}^{\infty} \kappa_\nu(\rho, T, Y_e) \rho(R') dR' = 2/3,$$

where the integration is carried out along a radial ray. At 15 MeV, near where the ν_e and $\bar{\nu}_e$ energy distributions at infinity peak, matter and neutrinos decouple at a radius of ~ 80 km at $t = 50$ ms, decreasing at later times to ~ 30 km. Note that the neutrinospheric radius becomes less and less dependent on the neutrino energy as time proceeds, which results from the steepening density gradient with increasing time (compare the black and red curves in the top left panel of Fig. 5). This lower-limit on the neutrinospheric radius of 30 km is to be compared with the 10–20 km radii where PNS convection obtains. The “saddle” region of very low Y_e at ~ 30 km, which harbors a very modest radial velocity at all times and, thus, hangs steady, does not let any material penetrate through.

Figure 14 depicts the neutrino luminosities until 300 ms after bounce, showing, after the initial burst of the ν_e luminosity, the rise and decrease of the $\bar{\nu}_e$ and “ ν_μ ” luminosities between 50 and 200 ms after core bounce. Compared to 1D simulations with SESAME for the same progenitor (Thompson et al. 2003), the $\bar{\nu}_e$ and “ ν_μ ” luminosities during this interval are larger by 15% and 30%, respectively. Moreover, in the alternate model using a transition radius at 30 km, we find enhancements of the same magnitudes and for the same neutrino species, but occurring ~ 50 ms earlier. This reflects the influence of the additional seeds introduced by the horns located right in the region where PNS convection obtains. We can thus conclude that the 15% and 30% enhancements in the $\bar{\nu}_e$ and “ ν_μ ” luminosities between 50 and 200 ms after core bounce observed in our baseline model are directly caused by the PNS convection.

There is evidence in the literature for enhancements of similar magnitude in post-maximum neutrino luminosity profiles, persisting over ~ 100 ms, but associated

with large modulations of the mass accretion rate, dominating the weaker effects of PNS convection. In their Fig. 39, Buras et al. (2005) show the presence of a ~ 150 ms wide bump in the luminosity of all three neutrino flavors in their 2D run (the run with velocity terms omitted in the transport equations). Since this model exploded after two hundred milliseconds, the decrease in the luminosity (truncation of the bump) results then from the reversal of accretion. Similar bumps are seen in the 1D code VERTEX (Rampp & Janka 2002), during the same phase and for the same duration, as shown in the comparative study of Liebendorfer et al. (2005), but here again, associated with a decrease in the accretion rate. In contrast, in their Fig. 10b, the “ ν_μ ” luminosity predicted by AGILE/BOLTZTRAN (Mezzacappa & Bruenn 1993; Mezzacappa & Messer 1999; Liebendorfer et al. 2002, 2004) does not show the post-maximum bump, although the electron and anti-electron neutrinos luminosities do show an excess similar to what VERTEX predicts. These codes are 1D and thus demonstrate that such small-magnitude bumps in neutrino luminosity may, in certain circumstances, stem from accretion. Our study shows that in this case, the enhancement, of the $\bar{\nu}_e$ and “ ν_μ ” luminosities, albeit modest, is due to PNS convection.

From the above discussion, we find that PNS convection causes the ~ 200 ms-long 10–30% enhancement in the post-maximum $\bar{\nu}_e$ and “ ν_μ ” neutrino luminosities in our baseline model, and thus we conclude that there is no sizable or long-lasting convective boost to the ν_e and $\bar{\nu}_e$ neutrino luminosities of relevance to the neutrino-driven supernova model, and that what boost there may be evaporates within the first ~ 200 ms of bounce.

4.2. Doubly-diffusive instabilities

When the medium is stable under the Ledoux criterion, Bruenn, Raley, & Mezzacappa (2005) argue for the potential presence in the PNS of doubly-diffusive instabilities associated with gradients in electron fraction and entropy. Whether doubly-diffusive instabilities occur is contingent upon the diffusion timescales of composition and heat, mediated in the PNS by neutrinos. Mayle & Wilson (1988) suggested that so-called “neutron fingers” existed in the PNS, resulting from the fast transport of heat and the slow-equilibration transport of leptons. This proposition was rejected by Bruenn & Dineva (1996), who argued that these rates are in fact reversed for two reasons. Energy transport by neutrinos, optimal in principle for higher-energy neutrinos, is less impeded by material opacity at lower neutrino energy. Moreover, because lepton number is the same for electron/anti-electron neutrinos *irrespective* of their energy, lepton transport is faster than that of heat. This holds despite the contribution of the other neutrino types (which suffer lower absorption rates) to heat transport.

Despite this important, but subtle, difference in diffusion timescales for thermal and lepton diffusion mediated by neutrinos, the presence of convection within the PNS, which operates on much smaller timescales (*i.e.*, ~ 1 ms compared to ~ 1 s), outweighs these in importance. In the PNS (a region with high neutrino absorption/scattering cross sections), the presence of convection operating on timescales of the order of a few milliseconds seems to dominate any doubly-diffusive instability asso-

ciated with the transport of heat and leptons by neutrinos. Furthermore, and importantly, we do not see overturning motions in regions not unstable to Ledoux convection. Hence, we do not, during these simulations, discern the presence of doubly-diffusive instabilities at all. This finding mitigates against the suggestion that doubly-diffusive instabilities in the first 300-500 milliseconds after bounce might perceptively enhance the neutrino luminosities that are the primary agents in the neutrino-driven supernova scenario.

4.3. Gravity waves

We have described above the presence of a region (C) with little or no inflow up to 100–300 ms past core bounce, which closely matches the location of minimum Y_e values in our simulations, whatever the time snapshot considered. At such times after core bounce, we clearly identify the presence of waves at the corresponding height of ~ 30 km, which also corresponds to the surface of the PNS where the density gradient steepens (see top-left panel of Fig. 5). As shown in Fig. 13, as time progresses, this steepening of the density profile causes the (deleptonizing) neutrinosphere to move inwards, converging to a height of ~ 30 –40 km, weakly dependent on the neutrino energy.

To diagnose the nature and character of such waves, we show in Fig. 15 the fluctuation of the latitudinal velocity (subtracted from its angular average), as a function of time and latitude, and at a radius of 35 km. The time axis has been deliberately reduced to ensure that the region under scrutiny does not move inwards appreciably during the sequence (Fig. 6). Taking a slice along the equator, we see a pattern with peaks and valleys repeated every ~ 10 –20 ms, with a smaller period at later times, likely resulting from the more violent development of the convection underneath the shock. We provide in Fig. 16 the angular-averaged temporal power spectrum of the latitudinal velocity (minus the mean in each direction). Besides the peak frequency at 65 Hz ($P \sim 15$ ms), we also observe its second harmonic at ~ 130 Hz ($P \sim 7.5$ ms) together with intermediate frequencies at ~ 70 Hz ($P \sim 14$ ms), ~ 100 Hz ($P \sim 10$ ms), ~ 110 Hz ($P \sim 9$ ms). The low frequencies at ~ 20 Hz ($P \sim 50$ ms), ~ 40 Hz ($P \sim 25$ ms) may stem from the longer-term variation of the latitudinal velocity variations.

Geometrically, as was shown in Figs. 2-4, the radial extent of the cavity where these waves exist is very confined, covering no more than 5–10 km around 35 km (at ~ 200 ms). In the lateral direction, we again perform a Fourier transform of the latitudinal velocity, this time subtracted from its angle average. We show the resulting angular power spectrum in Fig. 17 with a maximum at a scale of 180° (the full range), and power down to $\sim 30^\circ$. There is essentially no power on smaller scales, implying a much larger extent of the waves in the lateral direction than in the radial direction. We also decompose such a latitudinal velocity field into spherical harmonics in order to extract the coefficients for various l -modes. We show the results in Fig. 18, displaying the time-evolution of the coefficients for l up to 3, clearly revealing the dominance of $l=1$ and 2.

These characteristics are typical of gravity waves, whose horizontal k_h and vertical k_r wavenumbers are

such that $k_h/k_r \ll 1$. Moreover, the time frequency shown in (Fig. 16) corresponds very well to the frequency of the large-scale overturning motions occurring in the layers above, *i.e.*, $\nu_{\text{conv}} \sim v_{\text{conv}}/H_{\text{conv}} \sim 100$ Hz, since typical velocities are of the order of 5000 km s^{-1} and Δr between the PNS surface and the stalled shock is about 100 km. The behavior seen here confirms the analysis of Goldreich & Kumar (1990) on (gravity-) wave excitation by turbulent convection in a stratified atmosphere, with gravity waves having properties directly controlled by the velocity, size, and recurrence of the turbulent eddies generating them.

5. SUMMARY AND CONCLUSIONS

In this paper, we have presented results from multi-dimensional radiation hydrodynamics simulations of protoneutron star (PNS) convection, providing support for the notion that large-scale overturn of core regions out to and above the neutrinosphere does not obtain, in agreement with studies by, *e.g.*, Lattimer & Mazurek (1981), Burrows & Lattimer (1988), Keil et al. (1996), and Buras et al. (2005). Furthermore, the restricted convection is confined to a shell; no significant amount of neutrino energy from the diffusive inner regions makes it into the outer regions where neutrinos decouple from matter, thereby leaving the neutrino luminosity only weakly altered from the situation in which PNS convection does not occur.

We document our results by showing the spatial and time evolution for various thermodynamic and hydrodynamic quantities, with 1) stills sampling the first 300 ms past core bounce, 2) distribution functions, 3) time series, and 4) frequency spectra. In all simulations performed, convection occurs in two distinct regions that stay separate. While convection in the outer region shows *negative* average radial-velocities, implying systematic net accretion, it is associated in the inner region (radius less than 30 km) with zero time- and angle-averaged velocities. In the interface region between the two convection zones lies a region where the radial velocity at any time and along any direction is small. This effectively shelters the inner PNS from fierce convective motions occurring above 30 km during these epochs. In this interface region, we identify the unambiguous presence of gravity waves, characterized with periods of 17 ms and 8 ms, latitudinal wavelengths corresponding to 30 – 180° (at 35 km), and a radial extent of no more than 10 km.

The neutrinosphere radii, being highly energy dependent 50 ms after bounce (from 20 to ≥ 100 km over the 1–200 MeV range), become weakly energy-dependent 300 ms after bounce (20 to 60 km over the same range). At 15 MeV where the emergent $\nu_e/\bar{\nu}_e$ energy spectra peak at infinity, neutrinospheres shrink from ~ 80 km (50 ms) down to ~ 40 km (300 ms). This evolution results primarily from the mass accretion onto the cooling PNS, the cooling and neutronization of the accreted material, and the concomitant steepening of the density gradient.

Importantly, the locations of the ν_e neutrinospheres are at all times beyond the sites of convection occurring within the PNS, found here between 10 and 20 km. As a result, there is no appreciable convective enhancement in the ν_e neutrino luminosity. While energy is advected in the first ~ 100 ms to near the $\bar{\nu}_e$ and ν_μ neutrinospheres and there is indeed a slight enhancement of as much as

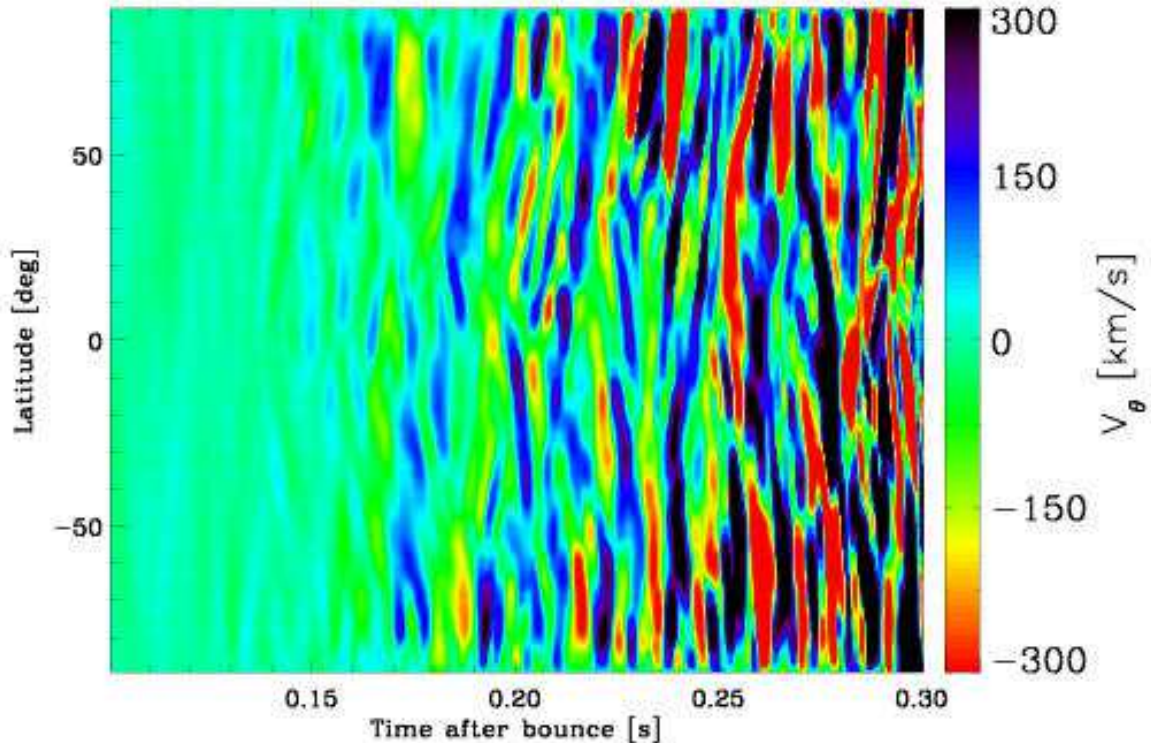


FIG. 15.— Color map of the latitudinal velocity (V_θ) as a function of time after bounce and latitude, at a radius of 35 km. We choose a time range of 200 ms, starting 100 ms after core bounce, to show the appearance, strengthening, and evolution to higher frequencies of gravity waves. Also, due to accretion/compression, the corresponding region recedes to greater depths with increasing time.

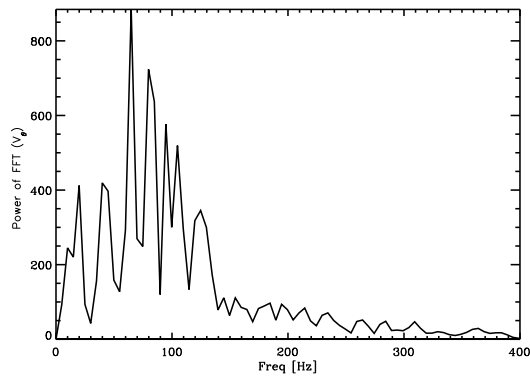


FIG. 16.— Temporal spectrum of the latitudinal velocity (V_θ) at a radius of 35 km, averaged over all directions, built from a sample of 401 frames equally spaced over the range 0.1–0.3 s past core bounce.

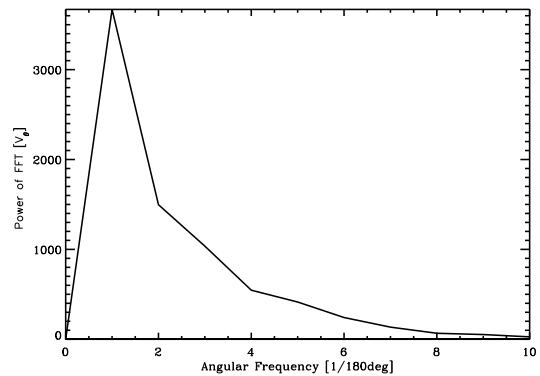


FIG. 17.— Angular spectrum of the Fourier Transform of the latitudinal velocity (V_θ) at a radius of 35 km, averaged over all times, built from a sample of 100 frames covering, with equal spacing, the angular extent of the grid.

$\sim 15\%$ and $\sim 30\%$, respectively, in the total $\bar{\nu}_e$ and ν_μ neutrino luminosities, after ~ 100 ms, this enhancement is choked off by the progressively increasing opacity barrier between the PNS convection zone and all neutrinospheres. Finally, we do not see overturning motions that could be interpreted as doubly-diffusive instabilities in regions not unstable to Ledoux convection.

We acknowledge discussions with and help from Rolf Walder, Jeremiah Murphy, Casey Meakin, Don Fisher,

Youssif Alnashif, Moath Jarrah, Stan Woosley, and Thomas Janka. Importantly, we acknowledge support for this work from the Scientific Discovery through Advanced Computing (SciDAC) program of the DOE, grant number DE-FC02-01ER41184 and from the NSF under grant number AST-0504947. E.L. thanks the Israel Science Foundation for support under grant # 805/04, and C.D.O. thanks the Albert-Einstein-Institut for providing CPU time on their Peyote Linux cluster. We thank Jeff Fookson and Neal Lauver of the Steward Com-

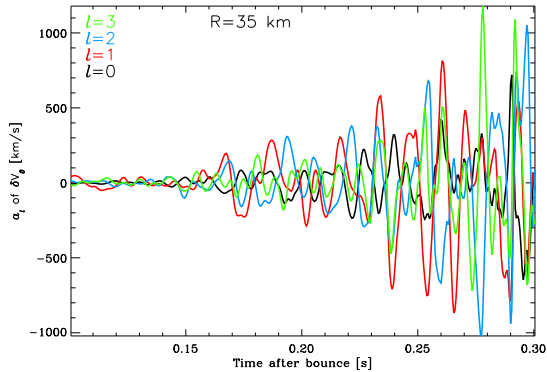


FIG. 18.— Time evolution after bounce of the spherical-harmonics coefficients for modes $l = 0$ (black), 1 (red), 2 (blue), and 3 (green) at a radius $R = 35$ km, given by $a_l = 2\pi \int_0^\pi d\theta \sin\theta Y_l^0(\theta) \delta v_\theta(R, \theta)$.

puter Support Group for their invaluable help with the local Beowulf cluster and acknowledge the use of the NERSC/LBNL/seaborg and ORNL/CCS/cheetah machines. Movies and still frames associated with this work can be obtained upon request.

APPENDIX

2D FLUX-LIMITED MULTI-GROUP DIFFUSION OF NEUTRINOS

The MGFLD implementation of VULCAN/2D is fast and uses a vector version of the flux limiter found in Bruenn (1985) (see also Walder et al. 2005). Using the MGFLD variant of VULCAN/2D allows us to perform an extensive study that encompasses the long-term evolution of many models. However, one should bear in mind that MGFLD is only an approximation to full Boltzmann transport and differences with the more exact treatment will emerge in the neutrino semi-transparent and transparent regimes above the PNS surface. Nevertheless, inside the neutrinosphere of the PNS the two-dimensional MGFLD approach provides a very reasonable representation of the multi-species, multi-group neutrino radiation field.

The evolution of the radiation field is described in the diffusion approximation by a single (group-dependent) equation for the average intensity J_g of energy group g with neutrino energy ε_g^a :

$$\frac{1}{c} \frac{\partial J_g}{\partial t} - \text{div}(D_g \nabla J_g) + \sigma_g^a J_g = S_g, \quad (\text{A1})$$

where the diffusion coefficient is given by $D_g = \frac{1}{3\sigma_g}$ (and then is flux-limited according to the recipe below), the total cross section is σ_g (actually total inverse mean-free-path), and the absorption cross section is σ_g^a . The source term on the RHS of eq. (A1) is the emission rate of neutrinos of group g . Note that eq. (A1) neglects inelastic scattering between energy groups.

The finite difference approximation for eq. (A1) consists of cell-centered discretization of J_g . It is important to use cell-centered discretization because the radiation field is strongly coupled to matter and the thermodynamic matter variables are cell-centered in the hydrodynamical scheme. The finite difference approximation of eq. (A1) is obtained by integrating the equation over a cell. Omitting group index and cell index one gets :

$$V \left[\frac{1}{c\Delta t} (J^{n+1} - J^n) + \sigma_g^a J^{n+1} \right] + \Sigma d\mathbf{S}_i \cdot \mathbf{F}_i^{n+1} = V S_g. \quad (\text{A2})$$

Here V is the volume of the cell, $d\mathbf{S}_i$ is the face-centered vector “ $area_i \mathbf{n}_i$,” \mathbf{n}_i being the outer normal to face i . The fluxes \mathbf{F}_i at internal faces are the face-centered discretization of

$$\mathbf{F}_i = -D_i \nabla J^{n+1}, \quad (\text{A3})$$

where

$$D_i = FL \left[\frac{1}{3\sigma_i} \right]. \quad (\text{A4})$$

Our standard flux limiter, following Bruenn (1985) and Walder et al. (2005) is

$$FL[D] = \frac{D}{1 + D|\nabla J|/J} \quad (\text{A5})$$

and approaches free streaming when D exceeds the intensity scale height $J/|\nabla J|$. The fluxes on the outer boundary of the system are defined by free streaming outflow and not by the gradient of J . Note that in eq. (A3) the fluxes are defined as face quantities, so that they have exactly the same value for the two cells on both sides of that face. The resulting scheme is therefore conservative by construction. In order to have a stable scheme in the semi-transparent regions (large D_g) we center the variables in eq. (A2) implicitly. The fluxes, defined by the intensity at the end of the time step, couple adjacent cells and the final result is a set of linear equations. The matrix of this system has

the standard band structure and we use a direct LU solver to solve the linear system. For a moderate grid size the solution of a single linear system of that size does not overload the CPU.

In order to handle many groups, we have parallelized the code according to groups. Each processor computes a few groups, usually less than 3, and transfers the needed information to the other processors using standard MPI routines. Since we do not split the grid between processors, the parallelization here is very simple. In fact, each processor performs the hydro step on the entire grid. In order to avoid divergent evolution between different processors due to accumulation of machine round-off errors, we copy the grid variables of one chosen processor (processor 0) onto those of the other processors, typically every thousand steps.

REFERENCES

- Browning, M.K., Brun, A.S., & Toomre, J. 2004, ApJ, 629, 461
 Bruenn, S.W. 1985, ApJS, 58, 771
 Bruenn, S.W., Buchler, J.R., & Livio, M. 1979, ApJ, 234, 183
 Bruenn, S.W. & Dineva, T. 1996, ApJ, 458, L71
 Bruenn, S.W., Raley, E.A., & Mezzacappa, A. 2005, astro-ph/0404099
 Buras, R., Rampp, M., Janka, H.-Th., & Kifonidis, K. 2005, astro-ph/0507135
 Burrows, A. 1987, ApJ, 318, 57
 Burrows, A., Hayes, J., & Fryxell, B.A. 1995, ApJ, 450, 830
 Burrows, A. & Goshy, J. 1993, ApJ, 416, 75
 Burrows, A. & Lattimer 1988, Physics Reports, 925, 51
 Epstein, R.I. 1979, Mon. Not. R. Astro. Soc., 188, 305
 Goldreich, P., & Kumar, P. 1990, ApJ, 363, 694
 Janka, H.-T. & Müller, E. 1996, Astron. Astrophys. , 306, 167
 Keil, W., Janka, H.-T., & Müller 1996, ApJ, 473, 111
 Lattimer, J.M. & Mazurek, T.J. 1981, ApJ, 246, 955
 Ledoux, P. 1947, ApJ, 105, 305
 Liebendorfer, M., Rosswog, S.K., & Thielemann, F.-K 2002, ApJS, 141, 229
 Liebendorfer, M., Messer, O.E.B., Mezzacappa, A., Bruenn, S.W., Cardall, C.Y., & Thielemann, F.-K 2004, ApJS, 150, 263
 Livio, M., Buchler, J.R., & Colgate, S.A. 1980, ApJ, 238, L139
 Livne, E. 1993, ApJ, 412, 634
 Livne, E., Burrows, A., Walder, R., Thompson, T.A., & Lichtenstadt, I. 2004, ApJ, 609, 277
 Mayle, R. & Wilson, J. R. 1988, ApJ, 334, 909
 Mezzacappa, A., & Bruenn, S.W. 1993, ApJ, 405, 669
 Mezzacappa, A., & Messer, O.E.B. 1999, J. Comput. Appl. Math., 109, 281
 Mezzacappa, A., Calder, A.C., Bruenn, S.W., Blondin, J.M., Guidry, M.W., Strayer, M.R., & Umar, A.S. 1998, ApJ, 493, 848
 Ott, C.D., Burrows, A., Livne, E., & Walder, R. 2004, ApJ, 600, 834
 Ott, C.D., Burrows, A., Thomspson, T.A., & Livne, E. 2005, submitted to ApJ
 Rampp, M., & Janka, H.-Th 2002, Astron. Astrophys. , 396, 361
 Smarr, L., Barton, S., Bowers, R.L., Wilson, J.R., 1981, ApJ, 246, 515
 Swesty, F.D., & Myra, E.S. 2005, astro-ph/0506178
 Swesty, F.D., & Myra, E.S. 2005, astro-ph/0507294
 Thompson, T.A., Burrows, A., & Pinto, P.A. 2003, ApJ, 592, 434
 Walder, R., Burrows, A., Ott, C.D., Livne, E., Lichtenstadt, I., & Jarrah, M. 2005, ApJ, 626, 317
 Wilson, J.R. & Mayle, R.W., 1993, Phys. Repts., 227, 97
 Woosley, S.E. & Weaver, T.A. 1995, ApJS, 101, 181